

## Impact of a discretization scheme on an autoignition time in LES of a reacting droplet-laden mixing layer

J. STEMPKA, Ł. KUBAN, A. TYLISZCZAK

*Department of Thermal Machinery, Czestochowa University of Technology,  
Faculty of Mechanical Engineering and Computer Science, Armii Krajowej 21,  
42-201 Czestochowa, Poland, e-mail: atyl@imc.pcz.pl*

WE ANALYSE AN AUTOIGNITION PROCESS IN A TWO-PHASE FLOW in a temporally evolving mixing layer formed between streams of a cold liquid fuel (heptane at 300 K) and a hot oxidizer (air at 1000 K) flowing in opposite directions. We focus on the influence of a discretization method on the prediction of the autoignition time and evolution of the flame in its early development phase. We use a high-order code based on the 6th order compact difference method for the Navier–Stokes and continuity equations combined with the 2nd order Total Variation Diminishing (TVD) and 5th order Weighted Essentially Non-Oscillatory (WENO) schemes applied for the discretization of the advection terms in the scalar transport equations. The obtained results show that the autoignition time is more dependent on the discretization method than on the flow initial conditions, i.e., the Reynolds number and the initial turbulence intensity. In terms of mean values, the autoignition occurs approximately 15% earlier when the TVD scheme is used. In this case, the ignition phase characterizes a sharp peak in the temporal evolution of the maximum temperature. The observed differences are attributed to a more dissipative character of the TVD scheme. Its usage leads to a higher mean level of the fuel in the gaseous form and a smoother distribution of species resulting in a lower level of the scalar dissipation rate, which facilitates the autoignition process.

**Key words:** autoignition process, two-phase flow, mixing layer.

Copyright © 2021 by IPPT PAN, Warszawa

### 1. Introduction

WITH THE RAPID DEVELOPMENT OF POWERFUL COMPUTERS, recent designs of practical devices often rely on mathematical modelling and numerical simulations with the conviction that errors introduced by discretization methods are small. However, in some problems, the obtained results can be largely influenced by a numerical method. For example, in modelling of the reactive flows, even small differences resulting from the discretization of the convective and diffusive terms in the scalar transport equations (temperature, species) can lead to substantial differences in the results caused by strongly nonlinear source terms. From that perspective, as the margin between correct and false results is very narrow, a proper choice of the numerical scheme is mandatory for obtaining re-

liable results. Unfortunately, in prototyping new devices the choice of appropriate numerical models, discretization schemes and boundary conditions become quite cumbersome since reference results for validation often do not exist. In such cases, a typical strategy is to apply a numerical method that proved its reliability either for similar cases or based on simplified benchmark problems. They, however, usually cover only some specific range of conditions, which are not necessarily consistent with the ones actually considered. Therefore, it can be risky to assume how the scheme performs if conditions change from the ones for which a particular numerical scheme was validated.

An impact of the discretization scheme was addressed, in many studies, in the past. For example in [1] the authors investigated the sensitivity of the large-scale ocean circulation models on the choice of a numerical advection scheme. It was found that the central-difference scheme leads to non-physical oscillations of temperature and salinity distributions. The upwind scheme turned out to be the most diffusive one. The flux-corrected transport scheme with a constant diffusion provided the best accuracy among all tested. In [2] an influence of the finite difference schemes and sub-grid models on Large Eddy Simulation (LES) predictions of the turbulent flow around a bluff body was analysed. It was reported that in an under-resolved near-wall region of a separating boundary layer the central difference scheme suffered from stability problems. The upwind-biased schemes of the 3<sup>rd</sup> order and the Smagorinsky sub-grid eddy viscosity model yielded reasonable predictions of the sub-grid stresses in most parts of the flow. Further improvements were obtained by applying high-order difference schemes, increasing the resolution of the small-scale phenomena, and using dynamic sub-grid stress models. CHAUDHURI *et al.* [3] performed analyses of turbulent 2D spatially developing mixing layers interacting with a shock wave, using three different Weighted Essentially Non-Oscillatory (WENO) variants: third-order, fifth-order and Bandwidth Optimized (BWO). They found that for coarse meshes the 5th order WENO scheme with limiters introduces dispersion errors and is more dissipative than WENO-BWO. Regarding the reactive flows, GOUGEON *et al.* [4] applied the Monotone Integrated Large Eddy Simulation (MILES) approach for analysis of a diffusion type hydrogen jet flame. They found that the numerical dissipation introduced by the WENO scheme is of the same order as the dissipation originating from a sub-grid model in the classical LES approach. The Total Variation Diminishing (TVD) schemes with various limiters (Superbee, MUSCL, Limited Linear, UMIST) were compared in [5]. The simulations based on the Reynolds Averaged Navier–Stokes (RANS) approach were devoted to the analysis of a non-reacting evaporating spray. It was observed that a more diffusive turbulence model diminishes the impact of the applied numerical scheme. NGUYEN *et al.* [6] focused on the influence of the numerical dissipation in simulations of an engine’s in-cylinder combustion. They found that small flow scales

are the most affected by the discretization scheme. The impact of TVD and WENO schemes on the solution accuracy in LES of an autoignition process in a temporally evolving mixing layer (cold H<sub>2</sub>/hot air) was analysed in [7]. The authors found that the discretization scheme affects the ignition scenario only for a lower oxidizer temperature. For the higher ones, the ignition process turned out to be dominated by the chemical kinetics.

In the present work, we focus on the dependency of the results on the numerical method in the simulations of two-phase reactive flows where not only the mixing of scalar variables depends on the applied scheme, but also the evaporation process that drives the production of fuel in the gaseous form, and thus, the rates of the chemical reactions. In particular, it is shown that the use of different discretization schemes in the scalar transport equations can lead to significant differences in the autoignition delay times and instantaneous temperature levels. Two often used discretization schemes for the advection terms are applied, namely, the 2nd order TVD and the 5th order WENO. The simulations are conducted using an in-house LES code, which is based on a high-order compact difference (CD) discretization method applied for the Navier–Stokes and continuity equations. We analyse the autoignition process in a turbulent two-phase mixing layer developing between the fuel droplets (n-heptane) dispersed in a stream of the air at 300 K and stream of an oxidizer, the air at 1000 K.

## 2. Model formulation

We consider a low Mach number, reacting two-phase flow for which the continuity and Navier–Stokes equations complemented with the equation of state in the framework of the LES method are given as:

$$(2.1) \quad \frac{\partial \bar{\rho}}{\partial t} + \underbrace{\frac{\partial \bar{\rho} \tilde{u}_j}{\partial x_j}}_{\text{CD}} = \bar{S}_{mass},$$

$$(2.2) \quad \frac{\partial \bar{\rho} \tilde{u}_i}{\partial t} + \underbrace{\frac{\partial \bar{\rho} \tilde{u}_i \tilde{u}_j}{\partial x_j}}_{\text{CD}} = - \underbrace{\frac{\partial \bar{p}}{\partial x_i} + \frac{\partial \bar{\tau}_{ij}}{\partial x_j} + \frac{\partial \tau_{ij}^{sgs}}{\partial x_j}}_{\text{CD}} + \bar{S}_{m,i},$$

$$(2.3) \quad p_0 = \bar{\rho} R \tilde{T},$$

where the CD letters under the brackets denote that the particular terms in the equations were discretized using the compact difference method. The bars and tildes denote the LES and Favre filtered quantities. The symbols  $p_0$  and  $R$  stand for the thermodynamic pressure and the mixture gas constant, respectively. The variables:  $u, \rho, p, T$  denote the velocity, density, hydrodynamic pressure and temperature. The terms  $\bar{\tau}_{ij}$  and  $\tau_{ij}^{sgs}$  represent the viscous and the subgrid stress

tensors. The former one is defined as  $\bar{\tau}_{ij} = \mu \left( \frac{\partial \bar{u}_i}{\partial x_j} + \frac{\partial \bar{u}_j}{\partial x_i} \right) - \frac{2}{3} \mu \frac{\partial \bar{u}_k}{\partial x_k} \delta_{ij}$  and the latter one  $\tau_{ij}^{sgs} = 2\mu_{sgs} \tilde{S}_{ij}$  in which  $\tilde{S}_{ij}$  is the Favre filtered rate of strain and  $\mu_{sgs}$  is the subgrid scale viscosity, modelled using Vreman's model [8]. The source terms  $\bar{S}_{mass}$  and  $\bar{S}_{m,i}$  serve for the two-way coupling between the droplets and the gas phase [9].

The species mass fractions ( $Y_\alpha$ ) and the enthalpy ( $h$ ) transport equations are given by:

$$(2.4) \quad \frac{\partial \bar{\rho} \tilde{Y}_\alpha}{\partial t} + \underbrace{\frac{\partial \bar{\rho} \tilde{Y}_\alpha \tilde{u}_j}{\partial x_j}}_{\text{TVD or WENO}} = \underbrace{\frac{\partial}{\partial x_j} \left[ \left( \frac{\mu}{\sigma} + \frac{\mu_{sgs}}{\sigma_{sgs}} \right) \frac{\partial \tilde{Y}_\alpha}{\partial x_j} \right]}_{\text{CD}} + \bar{S}_\alpha + \overline{\bar{\rho} \dot{\omega}_\alpha(Y, h)},$$

$$(2.5) \quad \frac{\partial \bar{\rho} \tilde{h}}{\partial t} + \underbrace{\frac{\partial \bar{\rho} \tilde{h} \tilde{u}_j}{\partial x_j}}_{\text{TVD or WENO}} = \underbrace{\frac{\partial}{\partial x_j} \left[ \left( \frac{\mu}{\sigma} + \frac{\mu_{sgs}}{\sigma_{sgs}} \right) \frac{\partial \tilde{h}}{\partial x_j} \right]}_{\text{CD}} + \bar{S}_h,$$

where as before the CD, TVD and WENO under the brackets denote the applied discretization method. The subscript  $\alpha$  denotes the species index from 1 to  $N$ -species. The symbols  $\sigma$  and  $\sigma_{sgs}$  refer to the Prandtl/Schmidt number and its turbulent analogue. They are assumed equal to 0.7 and 0.9, respectively. The applied values are recommended in literature and used in various studies [10, 11]. The source terms  $\bar{S}_\alpha$  and  $\bar{S}_h$  are responsible for the production of the fuel vapour and the energy exchange between the gas phase and droplets of the liquid fuel. The position, velocity, temperature of the droplets and their evaporation rates are computed as in [12] following the formulation of MILLER *et al.* [13], which is discussed later. The terms  $\overline{\dot{\omega}_\alpha(Y, h)}$  are the production/destruction terms of the species and they are computed using the Implicit LES (ILES) approach [14] assuming that  $\overline{\dot{\omega}_\alpha(Y, h)} \approx \dot{\omega}_\alpha(\tilde{Y}, \tilde{h})$ . We consider a one-step global reaction  $\text{C}_7\text{H}_{16} + 11(\text{O}_2 + 3.76\text{N}_2) = 7\text{CO}_2 + 8\text{H}_2\text{O} + 41\text{N}_2$  with the reaction rate obtained from the Arrhenius formula given by:

$$(2.6) \quad \bar{\omega} = B [\tilde{X}_F] [\tilde{X}_{O_2}] \exp\left(-\frac{T_A(\tilde{\phi})}{\tilde{T}}\right),$$

where  $B = 2.4 \times 10^{14} \text{ cm}^3 \cdot \text{mol}^{-1} \cdot \text{s}^{-1}$  is the pre-exponential factor,  $[\tilde{X}_F]$ ,  $[\tilde{X}_{O_2}]$  are the molar concentrations of species and  $\tilde{T}$  denotes the temperature. The symbol  $T_A(\tilde{\phi})$  represents the activation temperature calculated applying the 'tuning' procedure as proposed in [15]. This procedure relies on expressing the activation temperature as a function of the local equivalence ratio ( $\tilde{\phi}$ ). For the  $n$ -heptane oxidation the following fitting formulas developed by RICHARDSON [16] are applied:

$$(2.7) \quad T_A(\phi)/T_{a0} = \begin{cases} 1 + 1.6948(\phi - 0.74)^2 & \text{if } \phi \leq 0.74, \\ 1 & \text{if } 0.74 < \phi \leq 1.13, \\ 1 + 0.0092(\phi - 1) + 0.9423(\phi - 1.13)^2 & \text{if } \phi > 1.13, \end{cases}$$

where the parameter  $T_{a0}$  is equal to 15000 K. Compared to detailed chemical schemes the one-step irreversible mechanisms show deficiencies stemming from neglecting intermediate species and the quasi-steady state assumption. Specifically, they tend to influence the induction time, laminar flame speed and strain rates at extinction. However, the ‘tuning’ procedure used in the current study is intended to eliminate these weaknesses. The increase of  $T_A(\tilde{\phi})$  in fuel-rich regions ( $\phi > 1.13$ ) mimics the correct depletion of radicals by a rapid fuel consumption within the reaction layer. For leaner mixtures  $T_A(\tilde{\phi})$  is fitted appropriately to yield a very good agreement of the flame speed and the critical strain rate [16]. We emphasise that the main point of the current study is to highlight the importance of the numerical schemes in simulations of reactive two-phase flows. A possible error introduced by the one-step chemical scheme is systematic, and therefore the model overall is able to highlight the differences in predictions of the autoignition delay time introduced by the discretization scheme.

## 2.1. Spray modelling

**2.1.1. Spray source terms.** The liquid droplets were modelled in the Lagrangian framework as the point sources of mass, momentum and energy. The liquid phase was coupled with the gas phase through the source terms appearing in Eqs. (2.1), (2.2), (2.4) and (2.5). They comprise of weighted sums of contributions from all droplets ( $N_p$ ) found in each computational cell divided by its volume, i.e.,  $\bar{S} = 1/V \sum_{p=1}^{N_p} \dot{S}_p$ . Here,  $V$  denotes the grid cell volume and  $p$  is the index of  $p$ -th droplet. The source terms are formulated as follow:

$$(2.8) \quad \bar{S}_{mass,p} = \bar{S}_{\alpha,p} = -\frac{d}{dt}(m_d)_p,$$

$$(2.9) \quad \bar{S}_{m,p} = -\frac{d}{dt}(m_d v_d)_p,$$

$$(2.10) \quad \bar{S}_{h,p} = -\frac{d}{dt}(m_d c_f T_d)_p,$$

where  $m_d$ ,  $v_d$ ,  $T_d$  are mass, velocity and temperature of the droplets, respectively. The symbol  $c_f$  denotes the specific heat capacity of the liquid fuel.

**2.1.2. Droplets transport.** The positions and velocities of the droplets were computed according to [13]:

$$(2.11) \quad \frac{d\mathbf{x}_d}{dt} = \mathbf{v}_d,$$

$$(2.12) \quad \frac{d\mathbf{v}_d}{dt} = \frac{f_d}{\tau_d}(\tilde{\mathbf{u}} - \mathbf{v}_d),$$

where  $\tilde{\mathbf{u}}$  is the gas phase velocity at the droplet position and  $\tau_d$  is the droplet relaxation time  $\tau_d = \rho_f D^2 / (18\mu)$ , where  $\rho_f$  denotes the liquid fuel density and  $D$  is the droplet diameter. The correction factor  $f_d$  defined based on the Schiller–Naumann correlation for the drag coefficient is given as [9]:

$$(2.13) \quad f_d = \begin{cases} 1 + 0.15 \text{Re}_d^{0.687}, & \text{Re}_d \leq 1000, \\ 11/600 \text{Re}_d, & \text{Re}_d > 1000, \end{cases}$$

where  $\text{Re}_d = \rho D |\tilde{\mathbf{u}} - \mathbf{v}_d| / \mu$  is the droplet Reynolds number. In the current simulations the dilute regime for the spray is assumed, i.e., the droplets do not mutually interact. That can be justified taking into account that the volume fraction occupied by the droplets is significantly lower than  $10^{-3}$  referred in the literature as the threshold value of the diluted regimes [9].

**2.1.3. Droplets evaporation.** The evaporation of the droplets was modelled using the rapid mixing model (“D<sup>2</sup>-law”) [18] following the formulation of MILLER *et al.* [13]. The instantaneous changes in their mass and temperature were calculated from the following equations:

$$(2.14) \quad \frac{dT_d}{dt} = \frac{1}{3\tau_d} \frac{\text{Nu}}{\text{Pr}} \frac{C_{p,g}}{C_{p,f}} (T - T_d) + \frac{L_v}{c_{p,f}} \frac{\dot{m}_d}{m_d},$$

$$(2.15) \quad \frac{dm_d}{dt} = \dot{m}_d = -\frac{\text{Sh}}{3\text{Sc}} \frac{m_d}{\tau_d} \ln(1 + B_M),$$

in which  $C_{p,f}$ ,  $C_{p,g}$  are the heat capacities of the liquid fuel and its vapour,  $L_v$  is the latent heat of evaporation and  $B_M$  denotes the Spalding mass transfer number. The Prandtl and Schmidt numbers were computed as  $\text{Pr} = \mu_g C_{p,g} / \lambda_g$  and  $\text{Sc} = \mu_g / \rho_g \Gamma_g$ , respectively, while the Nusselt (Nu) and Sherwood (Sh) numbers were calculated using correlations suggested by CLIFT *et al.* [19]. The symbols  $\Gamma_g$ ,  $\lambda_g$  and  $\mu_g$  represent the binary diffusion coefficient, thermal conductivity and dynamic viscosity. The subscript ( $g$ ) denotes the values calculated for the mixture of the fuel vapour and surrounding gas using “1/3 rule” [17].

## 2.2. Solution algorithm

The computations were performed using an in-house LES code SAILOR. The solution algorithm for Eqs. (2.1)–(2.5) is based on a predictor-corrector

approach combining the Adams–Bashforth and Adams–Moulton methods for the time integration and the projection method for the pressure-velocity coupling, details of which can be found in [20, 21].

The spatial discretization was performed on half-staggered meshes using: (i) the 6th order compact difference scheme (CD in Eqs. (2.1)–(2.5)) for all terms in the Navier–Stokes and the continuity equations, and also for the diffusion terms in the species transport equations; (ii) the 2nd order TVD or the 5th order WENO scheme for the convective terms in the scalar transport equations (TVD or WENO in Eqs. (2.4)–(2.5)). The equations for velocity, position, mass and temperature of the droplets were integrated in time with the Euler explicit method. The flow variables were interpolated on the droplets positions using the 4th order Lagrangian interpolation method while the sources of the momentum, mass and energy from the droplets were distributed on the grid points using 2nd order trilinear interpolation. The applied code was used and verified in numerous studies of non-reacting [22–26] and reacting flows [12, 27–31]. For example, in [27, 28] the spark ignition in  $H_2/N_2$ /air mixtures using the detailed chemical mechanism of  $H_2$  oxidation was analysed in the temporally evolving mixing layer. There, key characteristics of the development of the ignition kernel and successive flame propagation or stabilisation of the reaction zone were predicted very accurately. In [29] the excited flames were successfully computed, while in [30] the Cabra flame was analysed in detail. In two-phase reactive flow simulations [12] we compared the reacting spray jets lift-off heights against the experimental data reporting good agreement. Impact of the evaporation model on the results of modelling of the two-phase reacting jet was analysed in [31] using the same one-step chemistry as presently. Satisfactory agreement of the average velocity profiles was obtained and only the temperature in the far field region of the jet flame was overpredicted.

### 2.3. Discretization methods

Details of derivations of the compact difference schemes can be found in a seminal paper of LELE [32] or in other papers as the literature on this subject is very extensive. The combination of the discretization schemes for the derivative approximations on the collocated and half-staggered grids and the interpolation between these grids was discussed in [20]. Here, we only present details of the TVD and WENO schemes as their alternate use is the main topic of this paper.

**2.3.1. TVD scheme.** Assuming that  $f$  stands for a general variable and  $u$  denotes a convection velocity, the terms such as  $u \frac{\partial f}{\partial x}$  are discretized depending on the sign of  $u$ . With the nodes indexed by  $i = 1, 2, \dots, N$  and a uniform spacing  $h$

the derivative  $\partial f/\partial x$  is approximated as:

$$(2.16) \quad \left. \frac{\partial f}{\partial x} \right|_{x=x_j} = \frac{1}{h}(\hat{f}_{i+1/2} - \hat{f}_{i-1/2}),$$

where  $\hat{f}_{i+1/2}$  and  $\hat{f}_{i-1/2}$  are the values of the  $f$  function at  $x_{i\pm 1/2}$ . For  $u > 0$  they are computed as [33]:

$$(2.17) \quad \hat{f}_{i+1/2} = \left( 1 + \frac{1}{2}\Psi(r_{i-1/2}^+) - \frac{1}{2}\Psi(r_{i-3/2}^+)/r_{i-3/2}^+ \right) (f_i - f_{i-1}),$$

where  $r_{i-1/2}^+$  and  $r_{i-3/2}^+$  are ratios of consecutive variations of the function  $f$ :

$$(2.18) \quad r_{i-1/2}^+ = \frac{f_{i+1} - f_i}{f_i - f_{i-1}} \quad \text{and} \quad r_{i-3/2}^+ = \frac{f_i - f_{i-1}}{f_{i-1} - f_{i-2}}$$

and  $\Psi(r)$  is a limiter function. In the present work we apply the van Leer limiter defined as [33]:

$$(2.19) \quad \Psi(r) = \frac{r + |r|}{1 + |r|}.$$

The values of  $\hat{f}_{i-1/2}$  are computed in a similar way assuming shifting of the nodes by one to the left. In the case when  $u < 0$  the values of  $\hat{f}_{i+1/2}$  and  $\hat{f}_{i-1/2}$  are computed from the analogical formulas with the opposite signs, i.e.,  $\Psi(r_{i+1/2}^-)$  and  $\Psi(r_{i+3/2}^-)$ .

**2.3.2. WENO scheme.** In the case of the WENO scheme  $\hat{f}_{i+1/2}$  is computed as [34]:

$$(2.20) \quad \hat{f}_{i+1/2} = w_1 \hat{f}_{i+1/2}^{(1)} + w_2 \hat{f}_{i+1/2}^{(2)} + w_3 \hat{f}_{i+1/2}^{(3)},$$

where  $f_{i+1/2}^{(1,2,3)}$  are calculated based on the node values as:

$$(2.21) \quad \begin{aligned} \hat{f}_{i+1/2}^{(1)} &= \frac{1}{3}f_{i-2} - \frac{7}{6}f_{i-1} + \frac{11}{6}f_i, \\ \hat{f}_{i+1/2}^{(2)} &= -\frac{1}{6}f_{i-1} + \frac{5}{6}f_i + \frac{1}{3}f_{i+1}, \\ \hat{f}_{i+1/2}^{(3)} &= \frac{1}{3}f_i + \frac{5}{6}f_{i+1} - \frac{1}{6}f_{i+2}, \end{aligned}$$

where the nonlinear weights  $w_k$  are defined through the linear weights  $\gamma_k$  as:

$$(2.22) \quad w_k = \frac{\tilde{w}_k}{\sum_{k=1}^3 \tilde{w}_k}, \quad \tilde{w}_k = \frac{\gamma_k}{(\epsilon + \beta_k)^2}$$

with  $\gamma_k$  equal to  $\gamma_1 = 1/3$ ,  $\gamma_2 = 3/5$ ,  $\gamma_3 = 3/10$ , where the smoothing coefficients  $\beta_k$  are defined as:

$$(2.23) \quad \begin{aligned} \beta_1 &= \frac{13}{12}(f_{i-2} - 2f_{i-1} + f_i)^2 + \frac{1}{4}(f_{i-2} - 4f_{i-1} + 3f_i)^2, \\ \beta_2 &= \frac{13}{12}(f_{i-1} - 2f_i + f_{i+1})^2 + \frac{1}{4}(f_{i-1} - f_{i+1})^2, \\ \beta_3 &= \frac{13}{12}(f_i - 2f_{i+1} + f_{i+2})^2 + \frac{1}{4}(3f_i - 4f_{i+1} + 3f_{i+2})^2. \end{aligned}$$

The parameter  $\epsilon$  in Eq. (2.22) is equal to  $10^{-6}$  to avoid singularity. As in the case of the TVD scheme the values of  $\hat{f}_{i-1/2}$  are computed by shifting the nodes by one to the left, and when  $u < 0$ , the values  $\hat{f}_{i+1/2}$  and  $\hat{f}_{i-1/2}$  are computed from symmetric formulas with the opposite signs.

### 3. Configuration

The computational domain used in the present research is shown in Fig. 1. Its dimensions in the streamwise ( $x$ ), spanwise ( $y$ ) and transversal ( $z$ ) directions are  $L_x = 0.025$  m,  $L_z = 0.01$  m and  $L_y = 0.04$  m, respectively. The periodic boundary conditions are defined in the  $x$  and  $z$  directions and the moving isothermal walls are assumed at  $y = \pm L_y/2$ . The temporally evolving mixing layer is formed between two streams flowing in the opposite directions. The upper stream is a mixture of the fuel droplets ( $n$ -heptane at 300 K) carried by air and the lower stream is the hot oxidizer (air at 1000 K). The velocity profile is defined by a hyperbolic tangent function, which is often adopted in the modelling of the shear layer that constitutes close to the nozzle in jet type flows. It is given by  $u(y) = U \tanh(2y/\delta)$ , where  $U$  denotes a free stream velocity outside the mixing layer and  $\delta = 2U/|dU/dy|_{\max}$  is the vorticity thickness equal to 1 mm. The initial homogeneous isotropic turbulence fields (HIT) were superimposed on the initial flow field. It was generated according to the following energy spectrum:

$$(3.1) \quad E(k) = 16\sqrt{2/\pi} \frac{u_0^2}{k_0} \left(\frac{k}{k_0}\right)^4 e^{-2(\frac{k}{k_0})^2},$$

where  $u_0' = \sqrt{\langle u'u' \rangle}$  denotes the RMS value of the initial velocity fluctuations and  $k_0$  is an adjustable wave number allowing to generate the velocity field with the required Taylor length scale  $\lambda$ . The RMS value is calculated as  $u_0' = T_i U$  for an assumed turbulence intensity  $T_i$ . The values of the Reynolds numbers,  $Re_\delta = U\delta/\nu$  ( $\nu$  – the kinematic viscosity of the oxidizer) and  $Re_\lambda = u_0'\lambda/\nu$ , and corresponding to them initial turbulence intensities are given in Table 1. Initially, the droplets had a uniform size ( $D = 20 \mu\text{m}$ ) and they were randomly distributed

in the upper part of the domain. The initial mass loading was  $m_f = 0.00166$  g and the total number of droplets was equal to  $N_p = 584685$ . This resulted in the volume fraction occupied by the droplets approximately equal to 0.00025 which means that it could be assumed that the droplets did not interact with each other [9].

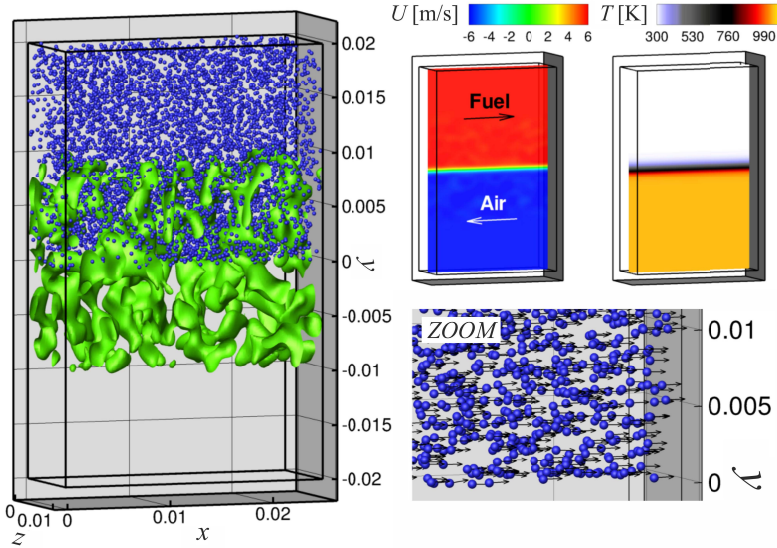


FIG. 1. Initial flow configuration inside the domain. Left figure: the spheres – denote the droplets positions, isosurfaces – spanwise velocity of the initial disturbances for  $Re_\delta = 25$  and  $T_i = 2\%$ . Right upper figures: the distribution of the streamwise velocity and the initial temperature field. Lower-right figure: the velocity vectors attached to the droplets.

The computational domain was discretized by  $120 \times 192 \times 48$  nodes distributed uniformly in the ‘x’, ‘y’ and ‘z’ directions respectively, resulting in the nodes spacings  $\Delta_{x,y,z} \approx 200 \mu\text{m}$ . Depending on the case the Kolmogorov length scale ( $\eta_K$ ) ranged from  $250 \mu\text{m}$  up to  $620 \mu\text{m}$ . Taking into account that with the applied settings the flow was only weakly turbulent ( $T_i < 10\%$ ) and the small flows scales vanished with time by dissipation, one could assume that the sub-grid velocity fluctuations were at a low level. That, along with the mesh density ensures almost DNS resolution was the necessary condition for the applicability of ILES approach [14]. Tests aiming at the examination of ILES model in a similar configuration as used in the present studies were performed in [27] and proved that ILES approach ensures reliable results. The diameters of the droplets in the current study were lower than the Kolmogorov length scale and 10 times smaller than the grid nodes spacings that justified treatment of the droplets as the point sources.

**Table 1. Nomenclature and characteristics of the initial velocity fields.**

Cases	$T_i$ [%]	$Re_\delta$	$Re_\lambda$	$u'_0$ [m/s]
2T25/2W25	2	25	0.4	$7.88 \cdot 10^{-3}$
4T25/4W25	4	25	0.8	$15.8 \cdot 10^{-3}$
6T25/6W25	6	25	1.2	$23.6 \cdot 10^{-3}$
2T50/2W50	2	50	0.8	$15.8 \cdot 10^{-3}$
4T50/4W50	4	50	1.6	$31.5 \cdot 10^{-3}$
6T50/6W50	6	50	2.4	$47.3 \cdot 10^{-3}$

In the present study, the impact of the discretization scheme was analysed by comparing the results obtained for 6 different setups of the initial flow conditions listed in Table 1. In each case, both TVD and WENO schemes were applied. In the following sections we refer to the particular case using abbreviations pointing the initial  $T_i$  and  $Re_\delta$ , and the letter ‘T’ or ‘W’ denoting the results obtained using TVD or WENO schemes. For instance, the label 2T25 denotes the results obtained for the case with  $T_i = 2\%$ ,  $Re_\delta = 25$  using TVD scheme. The analysed cases are listed in Table 1. The computations were carried out on a computer cluster using 24 CPUs. Assuming the CFL number equal to 0.1 the simulations of particular cases took approximately 48–96 hours. The differences in the solution times resulted from different values of the maximum velocity computed accordingly to  $Re_\delta$ .

## 4. Results

### 4.1. Reference time scale

In the following section, we analyse the dependence of the autoignition delay time on the discretization scheme and the flow initial conditions. As a reference value, we define the time delay before autoignition ( $\tau_{ref}$ ) obtained from the computations of the autoignition process in homogeneous heptane-air mixtures in a batch reactor with one-step global chemistry (the scheme used in the main body of the present study was based on the variable activation energy). The values of  $\tau_{ref}$  serve as an indication of the relative impact of the other processes present in the two-phase turbulent flow (e.g. evaporation, advection, mixing) that delay the autoignition. The  $\tau_{ref}$  is plotted in Fig. 2 as a function of mixture fraction ( $Z$ ) defined:

$$(4.1) \quad Z = \frac{\nu_{st} Y_F - Y_{O_2} + Y_{O_{2,2}}}{\nu_{st} Y_{F,1} + Y_{O_{2,2}}},$$

where  $\nu_{st}$  is the stoichiometric mass ratio,  $Y_F, Y_{O_2}$  are the local mass fractions of the heptane and oxygen and  $Y_{F,1}, Y_{O_{2,2}}$  are their initial mass fraction in the fuel

and oxidizer streams. In the present case the values  $Y_{F,1} = 1.0$  and  $Y_{O_2,2} = 0.233$  were assumed. The mass fractions of the mixture species are easily obtained for a given value of  $Y_F$  with  $Y_{O_2} = 0.233(1.0 - Y_F)$  and  $Y_{N_2} = 0.767(1.0 - Y_F)$ .

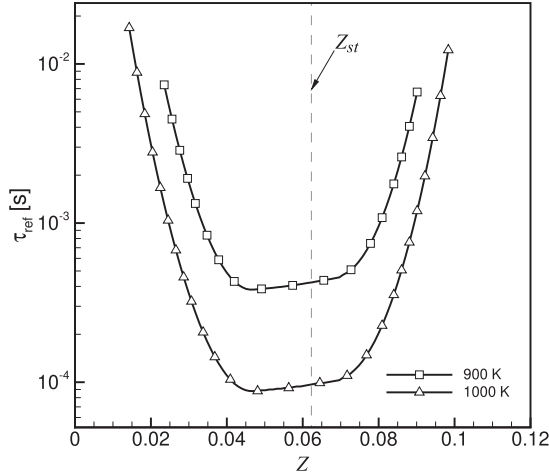


FIG. 2. Autoignition delay times for homogeneous heptane-air mixtures at  $T_{ini} = 900$  K and  $T_{ini} = 1000$  K for a range of  $Z$ .

The  $\tau_{ref}$  is calculated as a time period from the beginning of simulation to the time instance at which the maximum temperature ( $T_{max}$ ) increases 1% above the initial temperature. The mixture fraction at which  $\tau_{ref}$  is the smallest is called the most reactive [35] and is denoted as  $Z_{mr}$ . Comparing the solutions for the initial temperature  $T_{ini} = 900$  K and  $T_{ini} = 1000$  K it can be seen that  $Z_{mr} = 0.045$  is smaller than the stoichiometric mixture fraction  $Z_{st} = 0.061$ . Note that  $Z_{mr}$  is independent of temperature, however, the temperature strongly affects  $\tau_{ref}$ . For the case with  $T_{ini} = 900$  K it was equal  $\tau_{ref} = 0.4 \times 10^{-3}$  s and for  $T_{ini} = 1000$  K it was equal to  $\tau_{ref} = 0.09 \times 10^{-3}$  s. We refer to this value in the following subsections.

#### 4.2. Autoignition in the mixing layer

Prior to the autoignition the mixing layer, irrespective of the applied initial conditions, presents rather undisturbed character. The flow development at the stage directly preceding the autoignition is presented in Fig. 3. It shows the contours of the instantaneous temperature, fuel mass fraction and vorticity magnitude obtained for the cases characterized by  $Re_\delta = 25$  and  $T_i = 6$  using the TVD scheme (6T25, Fig. 3(a)) and the WENO scheme (6W25, Fig. 3(b)). It can be seen that at this stage the temperature and fuel mass fraction fields

in the centre of the domain are smooth. On the other hand, the formation of high vorticity regions makes the shear layer wavy. At later times it destabilizes and a number of individual vortices form. Comparing the solutions obtained using the TVD and WENO schemes it can be noted that the differences between the fields are hardly seen by the visual inspection. They become apparent only when the flow is more developed and the autoignition spots are present.

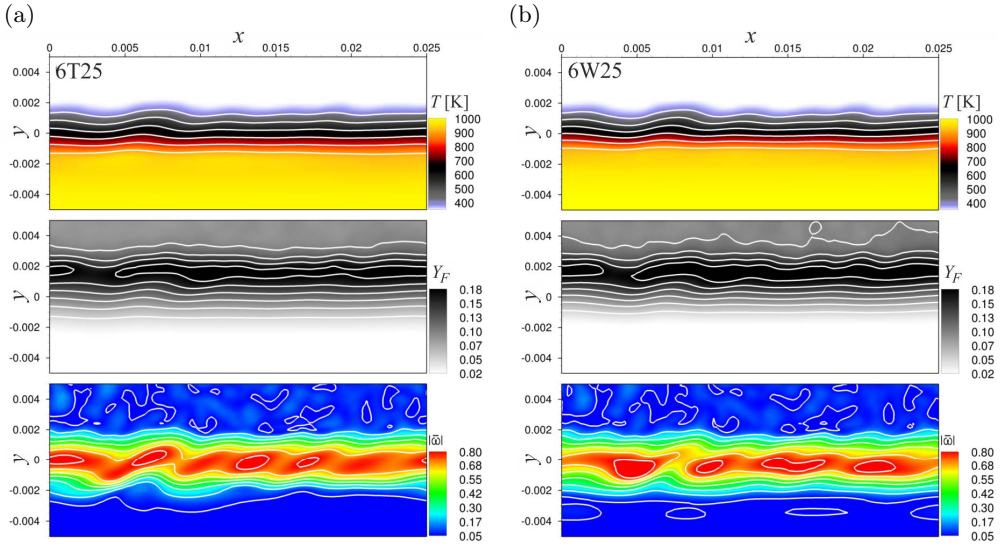


FIG. 3. Contours of instantaneous temperature, gaseous fuel mass fraction and vorticity magnitude, obtained for the cases (a) 6T25 and (b) 6W25 shortly before the autoignition.

The autoignition process sequence is depicted in Fig. 4 showing the results obtained from case 6W25. The subfigures present the results in subsequent time moments separated in time by  $0.35 \times 10^{-3}$  s. The red isosurface corresponds to the temperature equal to 1500 K. The spheres represent the droplets and their temperatures correspond to the colours shown in the legend. The gaseous fuel mass fraction field ( $Y_F \leq 0.25$ ) is coloured in light green, the black isolines with labels indicate distinct temperatures isovalues and the coloured lines reflect the vorticity field. As the heptane evaporates already in a room temperature, it can be seen that it is present on the upper side of the computational domain in a gaseous phase. However, its largest content is found in the region of the mixing layer where the droplets are heated by the lower stream of hot air. There, their temperature visibly increases and their sizes become smaller due to evaporation. The flame kernel appears on the lean side, and as is presented also in [35, 36], the autoignition reveals its local character. As the flame kernel grows causing

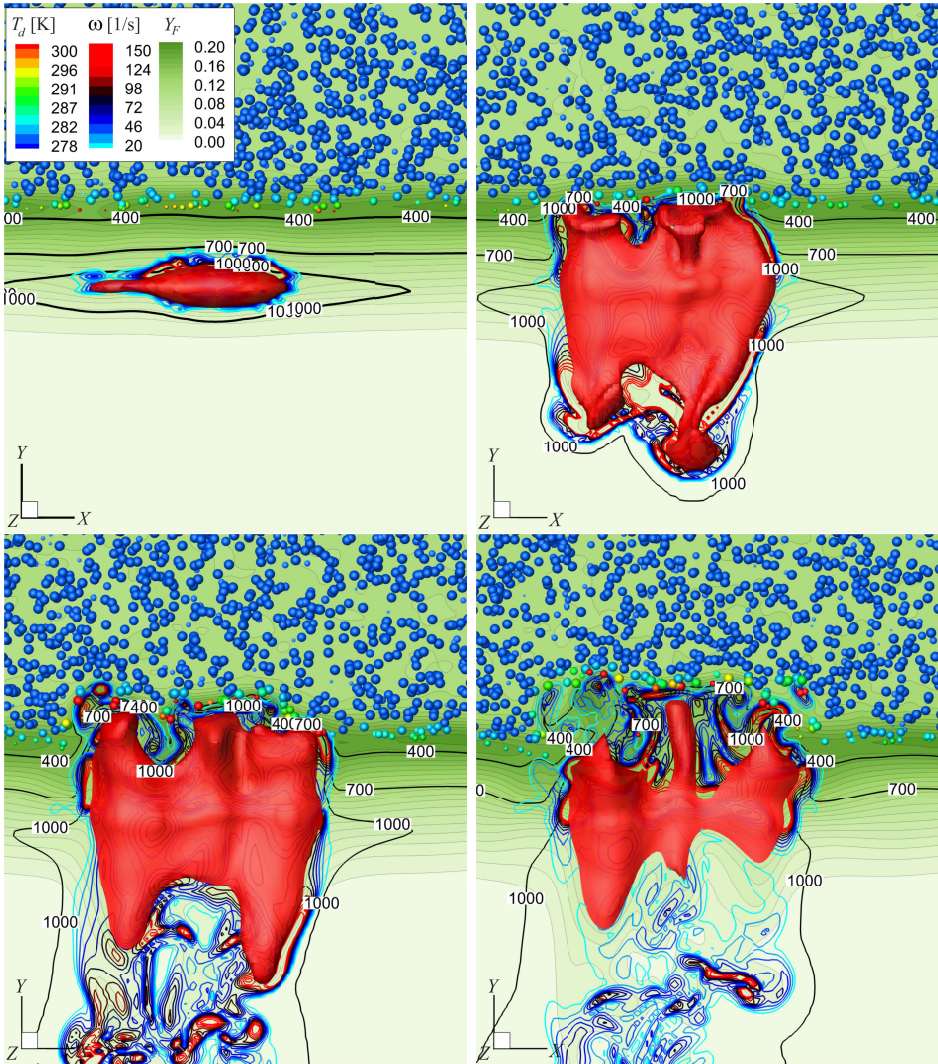


FIG. 4. Evolution of the localized autoignition event from case 6W25 presented at four consecutive time instances ( $t = 16.7, 16.9, 17.2$  and  $17.4$  ms). The subfigures show: the fuel mass fraction contours, vorticity magnitude isolines and temperature black isolines plotted in the middle section plane. Additionally, the isosurface of temperature equal to 1500 K and droplets represented by the spheres (enlarged) coloured by their respective temperatures are presented.

the expansion of hot gases towards the air stream in the negative  $y$ -direction the irregularities in the vorticity are induced. As there is no fuel on that side of the mixing layer the flame volume shrinks and starts expanding in the  $x$ - $z$  plane along the mixing layer.

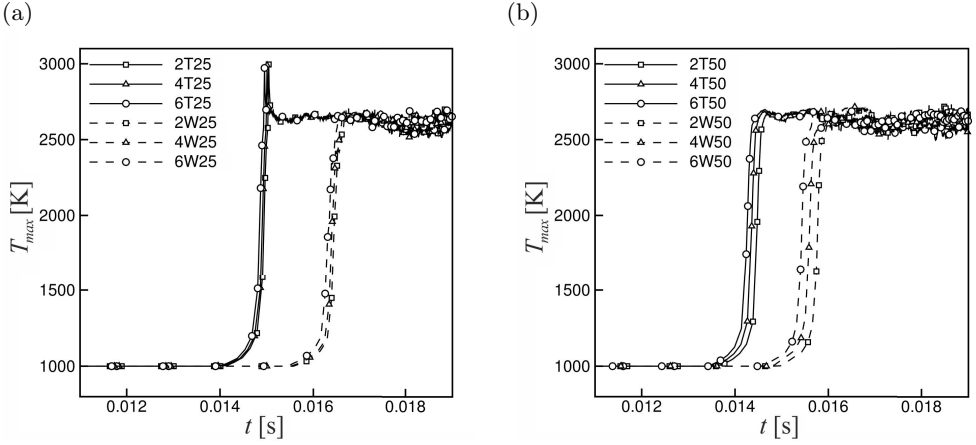


FIG. 5. Temporal evolution of  $T_{\max}$  for (a)  $Re_\delta = 25$  and (b)  $Re_\delta = 50$ .

The temporal evolution of the maximum temperature ( $T_{\max}$ ) for all analysed cases obtained for  $Re_\delta = 25$  and  $Re_\delta = 50$  is presented in Figs. 5(a) and (b), respectively. The ignition process is manifested by a sudden jump in the maximum temperature after which the temperature stabilizes at an approximately constant level. In the full-scale simulations the autoignition delay times are about two orders of magnitude longer comparing to  $\tau_{ref}$  in the homogeneous batch reactor (Fig. 2). Presently, the autoignition is delayed by the time needed for the evaporation of droplets and mixing of the evaporated fuel with the hot air stream. The rate of spray evaporation is strongly influenced by the temperature of a surrounding gas, which is distributed differently depending on initial conditions ( $Re_\delta, T_i$ ) and the applied discretization scheme. For instance, for the cases 2T25 and 2W25 at the time instance  $t = 10.0 \times 10^{-3}$  s the averaged temperatures and their RMS values in the central region of the mixing layer ( $y = \pm 0.5\delta$ ) are equal to  $\langle T \rangle_{WENO} = 711$  K,  $\langle T \rangle_{TVD} = 691$  K and  $T_{WENO}^{RMS} = 7.7$  K,  $T_{TVD}^{RMS} = 5.9$  K. Hence, knowing that in the mixing layer the flow conditions are not homogeneous, the mean temperatures and their maximum values are smaller compared to those assumed when computing  $\tau_{ref}$ , the fact that the autoignition occurs much later ( $\tau_{ign} \approx 15 \times 10^{-3}$  s) is not surprising. It can be seen that  $\tau_{ign}$  is shorter for the cases with  $Re_\delta = 50$  and it decreases with the increase of the turbulence intensity. However, the differences due to  $Re_\delta$  or  $T_i$  are much smaller than the differences resulting from the use of the TVD and WENO scheme. In the former case the averaged autoignition time is  $\tau_{ign} = 14.3 \times 10^{-3}$  s and in the latter one it is equal to  $\tau_{ign} = 15.5 \times 10^{-3}$  s. It should be noted that similar results were obtained for the cases run with different initial droplets distributions, which means that the observed differences are independent of the ran-

domness of the initial flow conditions but are caused by the use of the different numerical scheme. Taking into account that  $\langle T \rangle_{\text{TVD}} < \langle T \rangle_{\text{WENO}}$  it is somewhat unexpected that  $\tau_{ign}$  is shorter in case of using the TVD scheme. In the following sections, we try to find the reason why the TVD scheme accelerates the autoignition.

#### 4.3. Impact of discretization scheme on the evaporation process

Figure 6 shows the temporal evolution of the maximum value of the mixture fraction  $Z_{\max}$ , which can be directly related to the maximum of  $Y_F$  in the domain prior to the autoignition. As can be seen the results seem to be almost independent of  $Re_\delta$ . Its change causes only minor quantitative differences. They are definitively smaller than when the discretization scheme is changed. The  $Z_{\max}$  reaches  $Z_{mr} = 0.045$  in less than  $1.0 \times 10^{-3}$  s, but apparently the autoignition did not occur instantly after reaching this value. This suggests that the localisations of  $Z \geq Z_{mr}$  were outside the regime favourable for ignition being either in the region dominated by the strong shear stress or large strain rates as the main factors that prevent the autoignition [27, 28]. Worth noting is the fact that from the time instance  $t \approx 2.0 \times 10^{-3}$  s the values of  $Z_{\max}$  are approximately 5% larger for the WENO scheme for which the ignition occurs later. This means that the larger values of  $Z_{\max}$  or  $Y_{F,\max}$  do not imply faster ignition as one could intuitively expect.

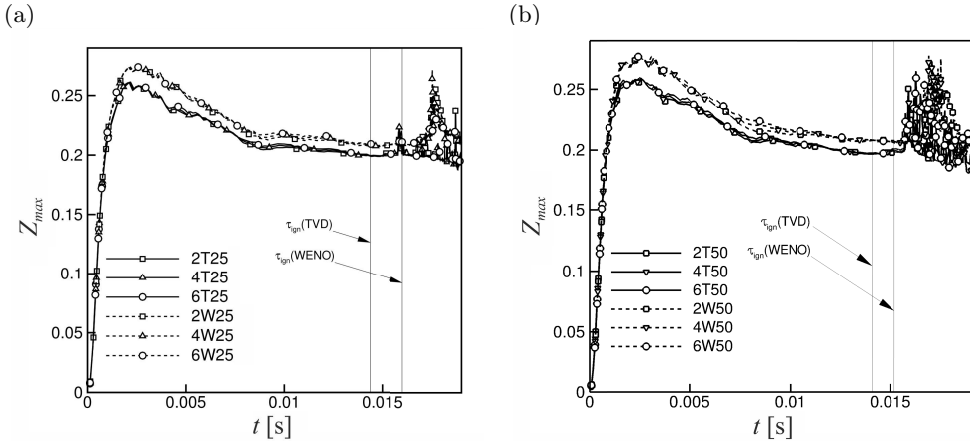


FIG. 6. Temporal evolution of  $Z_{\max}$  obtained with different schemes and values of the turbulence intensity. The results obtained for (a)  $Re_\delta = 25$  and (b)  $Re_\delta = 50$ . The average autoignition delay times obtained using both the schemes are indicated.

As a measure of an overall evaporation rate, we take an average value of the fuel mass fraction  $\langle Y_F \rangle$  in the region  $y = \pm\delta$ . The temporal evolution of  $\langle Y_F \rangle$

is presented for the results obtained using both TVD and WENO schemes for  $Ti = 2\%$  and  $Re_\delta = 25$  in Fig. 7(a) and  $Re_\delta = 50$  in Fig. 7(b). After an initial period ( $t > 5.0 \times 10^{-3}$  s) the amount of gaseous fuel increases almost linearly but this trend changes when the ignition occurs. After that moment  $\langle Y_F \rangle$  quickly rises, as the droplets close to the ignition kernel become engulfed by a developing flame and start to evaporate at the maximum rate. This takes place when the temperature surrounding the droplets is very high. In such conditions the droplets quickly reach the constant boiling temperature and the evaporation process is limited only by the mass transfer rate from the droplets to the gas phase.

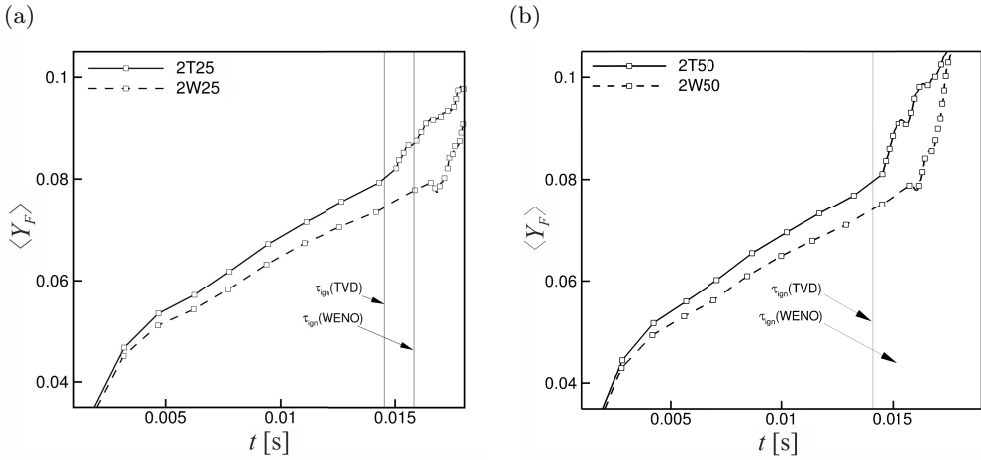


FIG. 7. Temporal evolution of  $\langle Y_F \rangle$  in the region  $y = \pm \delta$  obtained for (a)  $Re_\delta = 25$  and (b)  $Re_\delta = 50$ . The average autoignition delay times obtained with both schemes are indicated.

Regarding the impact of  $\langle Y_F \rangle$  on the ignition time, it seems that more intense evaporation observed in case of using the TVD scheme facilitates the ignition. It is interesting to note that the mean level of the fuel at  $\tau_{ign}$  is almost the same for the TVD and WENO schemes, it equals to  $\langle Y_F \rangle \approx 0.079$ . This may suggest that the necessary condition for the ignition is a certain minimum level of the fuel that is reached faster when the TVD scheme is used. However, taking into account that before the ignition process begins  $\langle Y_F \rangle = \langle Z \rangle > Z_{mr}$  such an explanation does not seem fully convincing. Rather, the obtained result confirms that the ignition is not conditioned exclusively on the mixture composition but is also affected by the flow conditions, as stated in [35]. Regarding the impact of  $Re_\delta$  it can be seen that it affects the evaporation process only after the ignition. For the higher  $Re_\delta$  the droplets evaporate faster.

#### 4.4. Impact of discretization scheme on the scalar dissipation rate

TVD scheme generally introduces a higher level of numerical diffusion than the WENO scheme, one can presume that the former leads to a smoother fuel distribution decreasing the value of the scalar dissipation rate ( $\chi$ ). The  $\chi$  in the present work was calculated assuming the local equilibrium for which the scalar variance is linked to the scalar dissipation rate through an algebraic expression  $\chi = 2D_t \frac{\partial Z}{\partial x_i} \frac{\partial Z}{\partial x_i}$  in which  $D_t = D/Sc_t$  is the turbulent diffusivity. This scalar dissipation rate reflects the magnitude of the strain rate that is related to the convective and diffusive terms in Eqs. (2.4)–(2.5). These terms compete with the chemical source terms and their large values can delay or even prevent the ignition [9, 35]. Figure 8 shows plots of the temporal evolution of the  $T_{\max}$  and scalar dissipation rate conditioned on  $T_{\max}$  (i.e.,  $\chi|T_{\max}$ ) for cases 2T25, 2W25 (Fig. 8(a)) and 2T50, 2W50 (Fig. 8(b)). The solid black and red lines correspond to the instantaneous values of  $T_{\max}$  obtained by applying the TVD and WENO schemes, respectively. Initially,  $T_{\max}$  belongs to the region on the oxidizer side where the gradients of  $Z$  are nearly zero, and hence  $\chi|T_{\max}$  are zero as well. When the autoignition spots appear, the maximum temperature occurs in the mixing layer region, where  $\nabla Z$ , and thus  $\chi|T_{\max}$  are large. It can be seen that for the WENO scheme  $\chi|T_{\max}$  has higher values and it varies much more than for the TVD scheme. The distribution of  $\chi|T_{\max}$  in the mixing layer region shortly before the autoignition also shows that for the TVD scheme its values are smaller. This means that the discretization scheme, which characterizes a larger numerical diffusion leads to a smoother spatial distribution of the fuel that along

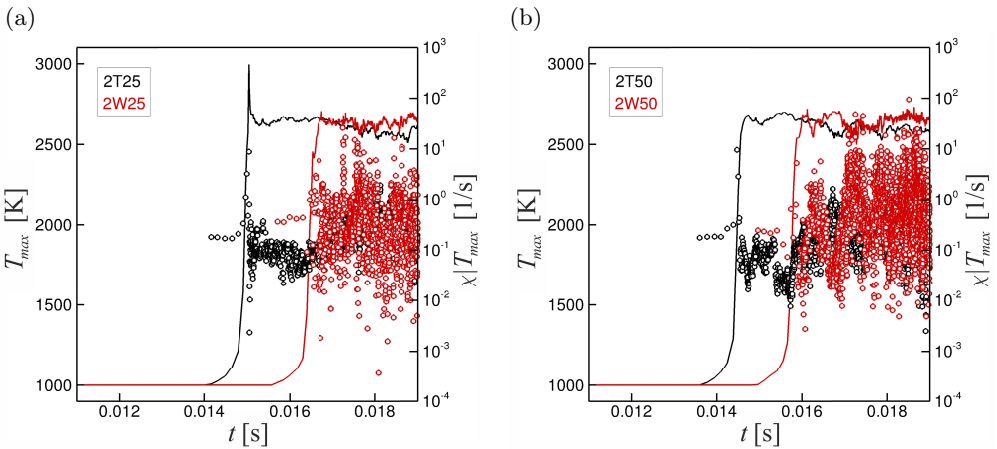


FIG. 8. Temporal evolution of  $T_{\max}$  (black and red lines) and  $\chi|T_{\max}$  (black and red points) corresponding to the cases (a) 2T25 and 2W25 and (b) 2T50 and 2W50.

with its higher mean level facilitates the ignition. Note, that these findings are valid for both Reynolds number values considered.

## 5. Conclusions

The paper presented comparative studies on the influence of the discretization scheme on the autoignition delay time in the reacting two-phase flow with the dispersed n-heptane droplets. The simulations were performed with the help of the high-order compact difference solver using both the TVD and WENO schemes to discretize the convective terms in the scalar transport equations. The obtained results showed the differences in the ignition times were dependent more on the discretization method than on the initial conditions, i.e., the Reynolds number or the initial turbulence intensity. When using the TVD scheme, the ignition always occurred earlier, approximately 2 ms, which translated to 15% of the average ignition time. In this case, the impact of the initial turbulence intensity was significantly smaller. Such behaviour was attributed to a larger level of the numerical diffusion, which affected the gradients of the fuel mass fraction and diminished differences resulting from the initial conditions. It was found that the TVD scheme leads to a smoother distribution of the fuel mass fraction and its larger mean values, and these factors accelerate the ignition. The fact that the numerical method has a larger influence on the solution than the physical conditions is not encouraging and should be considered as an important issue in the numerical investigations of the reactive flows. In general, it is difficult to univocally suggest which scheme ensures more accurate results and should be used. One should be aware that the formal order of the method does not necessarily mean better performance. It can happen that due to mutual interactions of discretization errors and sub-model errors (e.g., sub-grid viscosity or evaporation model) the low-order scheme may yield more accurate solutions. One can also expect that dependence of the results on the numerical scheme may vary from case to case. Hence, taking into account that availability of the experimental or DNS data, which could serve for validation, is often very limited, the assessment of the impact of the discretization scheme can be judged only by performing simulations using two or more numerical methods.

## Acknowledgements

This work was supported by the grant No. 2015/17/B/ST8/03217 (National Science Centre, Poland). Jakub Stempka received the financial support for this research within the framework of the doctoral grant No. 2019/32/T/ST8/00407 from the National Science Centre, Poland.

## References

1. R. GERDES, C. KÖBERLE, J. WILLEBRAND, *The influence of numerical advection schemes on the results of ocean general circulation models*, *Climate Dynamics*, **5**, 211–226, 1991.
2. A. NAKAYAMA, S. VENGADESAN, *On the influence of numerical schemes and subgrid-stress models on large eddy simulation of turbulent flow past a square cylinder*, *International Journal for Numerical Methods in Fluids*, **38**, 227–253, 2002.
3. A. CHAUDHURI, A. HADJADJ, A. CHINNAYYA, S. PALERM, *Numerical study of compressible mixing layers using high-order WENO schemes*, *Journal of Scientific Computing*, **47**, 170–197, 2010.
4. L. GOUGEON, I. FEDIOUN, *DNS/MILES of reacting Air/H<sub>2</sub> diffusion jets*, *Proceedings of the 6th International ERCOFTAC Work on Direct and Large-Eddy Simulation (University of Poitiers) (ERCOFTAC Series)*, 93–100, 2005.
5. F.P. KÄRRHOLM, F. TAO, *On performance of advection schemes in the prediction of diesel spray and fuel vapour distributions*, *Proceedings of the 22nd European Conference on Liquid Atomization and Spray Systems (Como Lake)*, paper ID ILASS08-2-12, 2008.
6. T. NGUYEN, A.M. KEMPF, *Investigation of numerical effects on the flow and combustion in LES of ICE*, *Oil & Gas Science and Technology*, **72**, 1–15, 2017.
7. A. ROSIAK, A. TYLISZCZAK, *Impact of numerical method on auto-ignition in a temporally evolving mixing layer at various initial conditions*, *Journal of Physics Conference Series*, **760**, 012027, 2016.
8. W. VREMAN, *An eddy-viscosity subgrid-scale model for turbulent shear flow: Algebraic theory and applications*, *Physics of Fluids*, **16**, 3670–3681, 2004.
9. P. JENNY, D. ROEKAERTS, N. BEISHUIZEN, *Modeling of turbulent dilute spray combustion*, *Progress in Energy and Combustion Science*, **38**, 846–887, 2012.
10. Y. TOMINAGA, T. STATHOPOULOS, *Turbulent Schmidt numbers for CFD analysis with various types of flow field*, *Atmospheric Environment*, **41**, 8091–8099, 2007.
11. A. TRIANTAFYLIDIS, E. MASTORAKOS, *Implementation issues of the conditional moment closure model in large eddy simulations*, *Flow, Turbulence and Combustion*, **84**, 481–512, 2010.
12. J. STEMPKA, A. TYLISZCZAK, *Impact of evaporation models and droplet size on auto-ignition and lift-off height in a spray jet flame*, *Combustion Science and Technology*, DOI: 10.1080/00102202.2019.1678843, 2019.
13. R.S. MILLER, K. HARSTAD, J. BELLAN, *Evaluation of equilibrium and non-equilibrium evaporation models for many-droplet gas-liquid flow simulations*, *International Journal of Multiphase Flow*, **24**, 1025–1055, 1998.
14. C. DUWIG, K.J. NOGENMYR, C. CHAN, M.J. DUNN, *Large eddy simulations of a piloted lean premix jet flame using finite-rate chemistry*, *Combustion Theory and Modelling*, **15**, 537–568, 2011.
15. E. FERNANDEZ-TARRAZO, A.L. SANCHEZ, A. LIÑAN, F.A. WILLIAMS, *A simple one-step chemistry model for partially premixed hydrocarbon combustion*, *Combustion and Flame*, **147**, 32–38, 2006.

16. E.S. RICHARDSON, *Ignition Modelling for Turbulent Non-Premixed Flows*, PhD thesis, Cambridge, 2007.
17. M.C. YUEN, L.W. CHEN, *On drag of evaporating liquid droplets*, *Combustion Science and Technology*, **14**, 147–154, 1976.
18. G.A.E. GODSAVE, *Studies of the combustion of drops in a fuel spray: the burning of single drops of fuel*, *Proceedings of the Combustion Institute*, **4**, 818–830, 1953.
19. R. CLIFT, J.R. GRACE, M.E. WEBER, *Bubbles, Drops and Particles*, Academic Press, New York, 1987.
20. A. TYLISZCZAK, *A high-order compact difference algorithm for half-staggered grids for laminar and turbulent incompressible flows*, *Journal of Computational Physics*, **276**, 438–467, 2014.
21. A. TYLISZCZAK, *High-order compact difference algorithm on half-staggered meshes for low Mach number flows*, *Computers & Fluids*, **127**, 131–145, 2016.
22. A. TYLISZCZAK, B.J. GEURTS, *Parametric analysis of excited round jets – numerical study*, *Flow, Turbulence and Combustion*, **93**, 221–247, 2014.
23. A. TYLISZCZAK, B.J. GEURTS, *Controlled mixing enhancement in turbulent rectangular jets responding to periodically forced inflow conditions*, *Journal of Turbulence*, **16**, 742–771, 2015.
24. J. STEMPKA, *Impact of subgrid modelling and numerical method on auto-ignition simulation of two-phase flow*, *Archives of Thermodynamics*, **39**, 55–72, 2018.
25. A. TYLISZCZAK, *Parametric study of multi-armed jets*, *International Journal of Heat and Fluid Flow*, **73**, 82–100, 2018.
26. A. BOGUSLAWSKI, K. WAWRZAK, A. TYLISZCZAK, *A new insight into understanding the Crow and Champagne preferred mode: a numerical study*, *Journal of Fluid Mechanics*, **869**, 385–416, 2019.
27. A. WAWRZAK, A. TYLISZCZAK, *Implicit LES study of spark parameters impact on ignition in a temporally evolving mixing layer between H<sub>2</sub>/N<sub>2</sub> mixture and air*, *International Journal of Hydrogen Energy*, **42**, 9815–9828, 2018.
28. A. WAWRZAK, A. TYLISZCZAK, *A spark ignition scenario in a temporally evolving mixing layer*, *Combustion and Flame*, **209**, 353–356, 2019.
29. A. TYLISZCZAK, *LES-CMC study of an excited hydrogen flame*, *Combustion and Flame*, **162**, 3864–3883, 2015.
30. A. TYLISZCZAK, *Assessment of implementation variants of conditional scalar dissipation rate in LES-CMC simulation of auto-ignition of hydrogen jet*, *Archives of Mechanics*, **65**, 97–129, 2013.
31. J. STEMPKA, L. KUBAN, A. TYLISZCZAK, *Influence of evaporation models on a lift-off height of a spray jet flame*, Tenth International Conference on Computational Fluid Dynamics (ICCFD10), Barcelona, Spain, July 9–13, 2018.
32. S.K. LELE, *Compact finite difference schemes with spectral-like resolution*, *Journal of Computational Physics*, **103**, 16–42, 1992.
33. C. HIRSCH, *Numerical Computation of Internal and External Flows*, Vol. 2, R.H. Gal- lagher, O.C. Zienkiewicz [eds.], John Wiley & Sons, Chichester, 1994.

34. C.W. SHU, *High-order finite difference and finite volume WENO schemes and discontinuous Galerkin methods for CFD*, International Journal of Computational Fluid Dynamics, **17**, 107–118, 2003.
35. E. MASTORAKOS, *Ignition of turbulent non-premixed flames*, Progress in Energy and Combustion Science, **35**, 57–97, 2009.
36. E. MASTORAKOS, *Forced ignition of turbulent spray flames*, Proceedings of the Combustion Institute, **36**, 2367–2383, 2017.

Received April 23, 2020; revised version November 3, 2020.

Published online April 7, 2021.

---